Remote Sensing of Environment 295 (2023) 113678

Contents lists available at ScienceDirect

Remote Sensing of Environment

journal homepage: www.elsevier.com/locate/rse

An approach to estimating forest biomass while quantifying estimate uncertainty and correcting bias in machine learning maps

Ethan Emick [a], Chad Babcock [a,*], Grayson W. White [b], Andrew T. Hudak [c], Grant M. Domke [d], Andrew O. Finley [b]

[a] University of Minnesota, Department of Forest Resources, St. Paul, MN 55108, USA
[b] Michigan State University, Department of Forestry, East Lansing, MI 48824, USA
[c] Rocky Mountain Research Station, USDA Forest Service, Moscow, ID 83843, USA
[d] Northern Research Station, USDA Forest Service, St. Paul, MN 55108, USA

ARTICLE INFO

Edited by Dr. Marie Weiss

Keywords:
Remote sensing
Bayesian hierarchical spatial modeling
Forest inventory
Carbon monitoring
Model-based inference
Design-based inference
Small area estimation
Machine learning
Random forest
Bias correction

ABSTRACT

Providing forest biomass estimates with desired accuracy and precision for small areas is a key challenge to incorporating forest carbon offsets into commodity trading programs. Enrolled forest carbon projects and verification entities typically rely on probabilistically sampled field data and design-based (DB) estimators to estimate carbon storage and characterize uncertainty. However, this methodology requires a large amount of field data to achieve sufficient precision and collection of these data can be prohibitively expensive. This has spurred interest in developing regional-scale maps of forest biomass that incorporate remote sensing data as an alternative to collecting expensive plot data. These maps are often generated using machine learning (ML) algorithms that combine remote sensing products and field measurements. While these maps can produce estimates across large geographic regions at fine spatial resolutions, the estimates are prone to bias and do not have associated uncertainty estimates. Here, we assess one such map developed by the National Aeronautics and Space Administration's Carbon Monitoring System. We consider model-assisted (MA) and geostatistical model-based (GMB) estimators to address map bias and uncertainty quantification. The MA and GMB estimators use a sample of field observations as the response, and the ML-produced map as an auxiliary variable to achieve statistically defensible predictions. We compare MA and GMB estimator performance to DB and direct (DR) estimators. This assessment considers both counties and a small areal extent experimental forest, all within Oregon USA. Results suggest the MA and GMB estimators perform similar to the DB estimator at the state level and in counties containing many field plots. But in counties with moderate to small field sample sizes, the GMB and MA estimators are more precise than the DB estimator. As within-county sample sizes get smaller, the GMB estimator tends to outperform MA. Results also show the DR estimator's state-level estimates are substantially larger than the DB, MA and GMB estimates, indicating that that the DR estimator may be biased. When assessing the GMB estimator for the experimental forest, we find the GMB estimator has sufficient precision for stand-level carbon accounting even when no field observations are available within the stand. Plot-level GMB uncertainty interval coverage probabilities were estimated and showed adequate coverage. This suggests that the GMB estimator is producing statistically rigorous uncertainty estimates.

1. Introduction

As global average temperatures continue to rise, it becomes increasingly important to implement strategies to mitigate climate change (IPCC, 2021). Forest carbon sequestration offers the potential to offset a substantial portion of anthropogenic CO_2 emissions (Houghton et al., 2009). Many state-level government entities and other organizations have established carbon markets that are designed, in part, to incentivize forest landowners to manage for carbon storage. For instance, the California Air Resources Board has set up a Compliance Offset Program that issues tradable credits to forest landowners based on the amount of carbon their enrolled forests store over time. The landowners can then sell their credits in California's Cap-and-Trade Program. Voluntary carbon trading markets that incorporate forest carbon

* Corresponding author.
E-mail address: cbabcock@umn.edu (C. Babcock).

https://doi.org/10.1016/j.rse.2023.113678
Received 2 February 2023; Received in revised form 4 May 2023; Accepted 5 June 2023

offset credits into their trading markets such as the Verra Verified Carbon Standard and the American Carbon Registry are also emerging (Streck, 2021). Under these types of carbon trading systems landowners manage forests to sequester carbon and, in turn, receive payments for the carbon their forests store over time.

It is essential to accurately monitor carbon sequestration and storage on forests enrolled in trading programs to correctly issue credits. Many carbon markets require forest carbon accrual to be estimated using strict design-based (DB) estimation protocols that often depend on a probability sample of field plots. Adhering to these strict DB estimation protocols can instill confidence in the carbon trading system as these estimators are often design-unbiased. However, for small landowners, conducting field inventories large enough to meet the carbon markets' precision demands can be cost prohibitive (Kerchner and Keeton, 2015). The earnings from selling credits in carbon trading markets often do not cover the cost of repeated inventories and other administrative costs associated with enrolling.

Forest carbon estimates can be directly and accurately derived from forest biomass estimates, and thus we will discuss forest carbon monitoring concurrently with forest biomass estimation. The incorporation of remote sensing data into forest carbon estimation procedures and monitoring efforts can decrease costs by, e.g., reducing the number of plots needed to measure or increasing the amount of time between repeat field measurements (Lister et al., 2020). Light detection and ranging (LiDAR) provides measurements of forest height and canopy density, which tend to be correlated with forest biomass (Hudak et al., 2012; Babcock et al., 2015; White et al., 2021). Vegetation indexes derived from optical data such as the normalized difference vegetation index are related to forest area and volume (Hall et al., 2006; Franklin et al., 1986). These relationships can be used to generate maps of forest biomass. Government agencies such as the National Aeronautics and Space Administration (NASA) and the United States Department of Agriculture (USDA) Forest Service make freely available remote sensing-based maps of forest biomass that landowners and auditing entities can use to monitor carbon (Silva et al., 2021; Huang et al., 2019; Blackard et al., 2008).

Machine learning (ML) algorithms, such as random forest, are often employed to predict and map forest biomass with remote sensing data (Mascaro et al., 2014; Chen et al., 2018; Urbazaev et al., 2018). Specifically, the random forest algorithm is able to ingest massive remote sensing datasets and find nuanced non-linear relationships between training observations of forest biomass and remote sensing covariates (Breiman, 2001; Hastie et al., 2009). Random forest requires no distributional assumptions and its internal sub-sampling procedures help safeguard against over-fitting when a large number of covariates are used in the modeling process (Segal, 2004; Olden et al., 2008).

Large training datasets are needed to effectively calibrate ML algorithms and produce accurate maps of forest biomass (Liu et al., 2018; Rogan et al., 2008). To overcome this hurdle, many research initiatives employ a forest inventory and remote sensing data crowd-sourcing strategy (Zhang and Liang, 2020; Duncanson et al., 2019; Hudak et al., 2020; Duncanson et al., 2022). This involves collecting a substantial number of project-level remote sensing (e.g., airborne LiDAR) and field inventory datasets to serve as training observations. Crowd-sourcing project-level datasets can be a great strategy to assemble a large number of training observations, but there are potential drawbacks. It is possible that specific locations or environmental conditions can be over- or under-represented in the crowd-sourced dataset. Also, different protocols for field plot setup and tree measurement can be used from project to project. These issues can lead to poor random forest model calibration and subsequent out-of-sample prediction (Millard and Richardson, 2015).

Model-assisted (MA) estimators can provide a framework to produce statistically defensible estimates using information from ML produced maps. MA estimators incorporate supplemental information into a DB estimation framework through an assisting model. In the current setting, the assisting model regresses forest biomass field measurements onto an ML map product. Recent literature in forest inventory has included the broad use of MA estimators with probabilistically sampled field plot data and remote sensing variables to estimate various forest inventory parameters (Saarela et al., 2015; Gregoire et al., 2011; Næsset, 2011; Strunk et al., 2014; McConville et al., 2020; Ekström and Nilsson, 2021; Frescino et al., 2022; Wojcik et al., 2022). Oftentimes, in areas of interest that have few field plots, MA estimators still cannot provide sufficient precision for meaningful inference about quantities of interest such as biomass (see, e.g. Frescino et al. (2022) Fig. 8).

To potentially increase precision further, we consider the model-based inferential paradigm where prediction at unobserved field sampling locations is informed, in part, by the ML map. Compared with the DB inferential paradigm, the validity of inference within the model-based setting relies on the posited model's distributional assumptions, rather than the sampling design.

Geostatistical model-based (GMB) estimators are a class of model-based estimators that explicitly accommodate extraneous spatial autocorrelation and help to adhere to the modeling assumptions needed to conduct valid model-based statistical inference (Babcock et al., 2018; Finley et al., 2013). GMB estimators do not share the same asymptotic guarantees concerning bias as estimators in a design-based paradigm such as the DB and MA estimators described above. However, previous studies have shown that fitting a GMB estimator with a probability sample of observations produces estimates similar to those produced from a DB estimator (Ver Hoef, 2002; Finley et al., 2011; Temesgen and Ver Hoef, 2015). An advantage of GMB estimators is that, unlike DB and MA estimators, no sample observations within the area of interest (AOI) are needed to generate estimates with associated uncertainty for that AOI. This advantage allows for statistically rigorous estimates and associated uncertainties down to the spatial resolution of the ML map (e.g., 30 m pixels).

Here, we explore the use of MA and GMB estimators that leverage ML-produced maps of aboveground biomass (AGB) and a probability sample of field plot data to estimate AGB density for a variety of AOIs in the state of Oregon. We test the candidate estimators using AGB maps made publicly available through NASA's Carbon Monitoring System (CMS) Program for the state of Oregon (Hudak et al., 2020). We use USDA Forest Service Forest Inventory and Analysis (FIA) field plot AGB values as training data in our candidate estimators. We compare the MA and GMB estimators to a direct (DR) estimator of AGB using the random forest AGB predictions alone and a traditional DB estimator that only incorporates FIA field plot data. We further examine the influence of field plot sample size and AOI extent on estimator uncertainty for the candidate estimators. We also examine plot-level GMB uncertainty interval coverage by calculating fitted-value and holdout-prediction coverage probabilities.

2. Methods

2.1. Study area

The study area includes all forested portions of Oregon. Forested areas were determined using the ALOS PALSAR forest/non-forest mask for the year 2009 (Shimada et al., 2014). Oregon sits in a longitudinal precipitation gradient, with annual precipitation being highest in the western portion of the state. Oregon contains three major mountain ranges; the Oregon Coast Range, Cascade Range and the Klamath Range. Oregon's forests are primarily evergreen, with 86% of the states forests being dominated by coniferous cover types (Bansal et al., 2017). Our AOIs are the entire study region (i.e., the state of Oregon), each of the 36 counties in Oregon, and the HJ Andrews Experimental Forest (HJA).

The HJA is a 6400 ha forest located in Lane County. It is jointly managed by the USDA Forest Service and Oregon State University. The elevation ranges from 410 to 1630 m. Douglas fir-western hemlock forests occupy low elevation sites and Pacific silver fir forests occupy

high elevation sites (https://andrewsforest.oregonstate.edu/).

2.2. Field data

We use the USDA FIA program's plot data for this analysis. Allometric equations found in the Forest Vegetation Simulator's (FVS) Fire and Fuels Extension module were used to estimate AGB for live and dead trees within plots with a diameter at breast height measurement $\geq$ 12.7 cm (5 in) (Reinhardt and Crookston, 2003). Tree-level estimates of AGB were summed to the plot level and divided by plot area to generate density estimates. The FIA dataset is a spatially balanced systematic sample where all plots have an equal probability of inclusion. FIA plots are sampled annually on a rotating panel system where individual plots are remeasured approximately every 10 years in western states (Bechtold and Patterson, 2005). There were ~940 forested FIA plots measured each year in Oregon from 2001 to 2016. The number of forested FIA plots measured annually in Oregon's counties ranged from 0 to ~95 depending on county size and proportion of forest area within the county.

2.3. Remote sensing-based aboveground biomass maps

Remote sensing-based AGB map products for the years 2001–2016 for the state of Oregon were produced as part of a stakeholder driven biomass mapping project for the western USA and were funded through NASA CMS (Hudak et al., 2020). We will refer to these maps as *CMS-AGB maps*. The CMS-AGB maps were created using the following multistep process. A random forest model was fit using stakeholder provided LiDAR and field plot datasets (Fekety et al., 2020). AGB predictions produced from this *project-level* random forest model were then stratified and randomly subsampled to produce a training dataset for a regional random forest model. Covariates used in the regional random forest model included Landsat time series metrics fit with the LandTrendr algorithm, climate metrics from Climate FVS, topographic information, and the Simard canopy height map (Kennedy et al., 2010; Simard et al., 2011).

There is a publicly available CMS-AGB map hosted on the ORNL Distributed Active Archive Center (Fekety and Hudak, 2019), which has been recalibrated to better align with regional FIA field plot data using a regression model. Details about the recalibration are given in Hudak et al. (2020). Because we are examining estimators that use FIA plot data as a response variable, our estimators employ the uncalibrated CMS-AGB maps described in Hudak et al. (2020) in effort to avoid any circular analysis and double dipping pitfalls (Kriegeskorte et al., 2010; Ball et al., 2020).

Perturbed FIA plot location data were used in all subsequent analyses. However, USDA Forest Service personnel extracted CMS-AGB map values for FIA plots using true locations before providing the perturbed location data for this analysis. This ensured that relationships between the FIA observations and CMS-AGB maps were retained.

2.4. Estimators

Four candidate estimators for AGB density are considered in this study. First, a DR estimator that uses only the CMS-AGB map values within the AOI to produce its estimate. Next, a DB estimator that uses only the FIA plots within the AOI to produce its estimate. Next, an MA estimator that uses FIA plots as the response and the CMS-AGB map as the auxiliary data, with ordinary least squares linear regression as the assisting model to produce its estimate. Finally, a GMB estimator that uses a spatial regression model with FIA plots as the response and the CMS-AGB map as auxiliary data to produce its estimate. The following subsections detail the specifics of each estimator, but first we introduce notation.

We let s, *the sample*, represent the sample of FIA field plots within the AOI, and U, *the universe*, represent every pixel within the AOI at the resolution of the CMS-AGB map. We use n as the number of FIA plots within the AOI, N as the number of CMS-AGB pixels within the AOI, and n^* as the number of FIA plots within the study area. We use x_i to denote the CMS-AGB map prediction at the ith pixel within the AOI and y_i to denote the AGB density at the ith FIA plot within the AOI. Specific to the GMB estimator, we use M to denote the number of Markov chain Monte Carlo (MCMC) samples, and l to index over the M MCMC samples. We also define $\boldsymbol{s}$ (i.e., a bold letter s) to be a 2-dimensional coordinate vector within the study area. Note that this $\boldsymbol{s}$ is different from s which was previously defined as the *sample*. Finally, given an estimator abbreviated *EST*, we denote the mean predicted value for AGB in an AOI as $\widehat{\bar{y}}_{EST}$.

A notable aspect of the estimators we are using is that while there are a finite number of pixels within the study region, we assume an infinite population paradigm. This paradigm aligns with FIA's choices, and with such a large population, the finite population correction factor would only make negligible changes to our results as it would be essentially one.

2.4.1. Direct estimator

The DR estimator uses the CMS-AGB map predictions to estimate AGB density (Mg/ha) and does not use field plot observations. The DR estimator for the AOI is

$$\widehat{\bar{y}}_{DR} = \frac{1}{N}\sum_{i\in U} x_i. \tag{1}$$

The DR estimator is simply the average of the CMS-AGB map grid cell values in the AOI. Because the probability sample of field observations is not incorporated into the DR estimator, it is not possible to derive an estimator for the standard error within a design- or model-based inferential paradigm.

2.4.2. Design-based estimator

The DB estimator uses the probability sample of field plot data to estimate AGB density. The CMS-AGB map predictions are not used in this estimator. The DB estimator for the AOI is

$$\widehat{\bar{y}}_{DB} = \frac{1}{n}\sum_{i\in s} y_i. \tag{2}$$

The variance estimator for the DB estimator is

$$\widehat{V}(\widehat{\bar{y}}_{DB}) = \frac{1}{n(n-1)}\sum_{i\in s}(y_i - \widehat{\bar{y}}_{DB})^2. \tag{3}$$

The upper and lower limits of the 95% confidence interval for the DB estimator can be obtained using

$$\widehat{\bar{y}}_{DB} \pm \Phi^{-1}(1-.95/2)\sqrt{\widehat{V}(\widehat{\bar{y}}_{DB})}, \tag{4}$$

where $\Phi^{-1}(\cdot)$ is the quantile function of the standard normal distribution.

2.4.3. Model-assisted estimator

The MA estimator used here is an extension of the most common class of MA estimator, the generalized regression (GREG) estimator (Cassel et al., 1976). The GREG uses a linear regression with coefficients estimated from data within the AOI as the assisting model for estimation. We extend the GREG to fit the linear regression over the entire study region (in our case, Oregon USA), rather than the AOI. In the literature, this is often referred to as the modified-GREG (Rao and Molina, 2015). We will refer to this estimator hence-forth as the MA estimator.

The MA estimator uses the probability sample of field plot data and the CMS-AGB map. An assisting model relates the field plot and CMS-AGB map data within the estimator. The MA estimator for the AOI is

$$\widehat{\bar{y}}_{MA} = \frac{1}{N}\sum_{i\in U}\widehat{y}_i + \frac{1}{n}\sum_{i\in s}(y_i - \widehat{y}_i), \tag{5}$$

where the assisting model used to calculate $\widehat{y}_i$ is

$$\widehat{y}_i = \widehat{\beta}_0 + \widehat{\beta}_1 x_i. \tag{6}$$

The coefficient estimates $\widehat{\beta}_0$ and $\widehat{\beta}_1$ are obtained using ordinary least squares regression based on *all observations within the study area*, n^*. This allows for larger sample sizes in the assisting model, which allows for more stable estimates of model parameters (see, e.g. Wojcik et al. (2022), Fig. 5) and better behavior of the variance estimator. The standard variance estimator of $\widehat{\bar{y}}_{MA}$ is

$$\widehat{V}(\widehat{\bar{y}}_{MA}) = \frac{1}{n(n-1)}\sum_{i\in s}(y_i - \widehat{y}_i)^2. \tag{7}$$

The MA estimator's variance estimator is asymptotically unbiased, however, the variance estimator tends to be negatively biased for models with many auxiliary variables and small sample sizes, as the variance estimator does not account for model estimation error (McConville et al., 2020). The variance estimator for the MA estimator has been found to be less negatively biased than the GREG variance estimator in similar forest inventory applications (Wojcik et al., 2022).

The upper and lower limits of the 95% confidence interval for the MA estimator can be obtained using

$$\widehat{\bar{y}}_{MA} \pm \Phi^{-1}(1 - .95/2)\sqrt{\widehat{V}(\widehat{\bar{y}}_{MA})}. \tag{8}$$

2.4.4. Geostatistical model-based estimator

Like the MA estimator, the GMB estimator uses the probability sample of field plot data and the CMS-AGB map predictions. However, being model-based, the GMB estimator does not explicitly require field plot observations to be probabilistically sampled as in the DB and MA estimators (Gregoire, 1998). While a probability sample is not needed with the GMB estimator, a field sample that is *representative* of the population is needed. The use of a sufficiently sized probability sample in the GMB estimator helps ensure that the sample is representative of the population (see McRoberts (2010)), and thus in this study we use a probability sample of field plot data. The GMB estimator uses a spatial regression model to relate the field plot and CMS-AGB map data. This model optimally weights observations from spatially proximate field plots to inform the estimate. The GMB estimate for the AOI and its associated variance are based on summaries of MCMC samples from Bayesian posterior distributions (Gelfand et al., 2003; Banerjee et al., 2014). The GMB estimator for the AOI is

$$\widehat{\bar{y}}_{GMB} = \frac{1}{M}\sum_{l=1}^{M}\widehat{\bar{y}}^{l}_{GMB} \tag{9}$$

with

$$\widehat{\bar{y}}^{l}_{GMB} = \frac{1}{N}\sum_{i\in U}\widetilde{y}^{l}(\boldsymbol{s}_i)_{GMB}, \tag{10}$$

where $\widetilde{y}^{l}(\boldsymbol{s}_i)$ is the l-th sample from the posterior predictive distribution (PPD) of AGB density at the i-th grid cell's spatial location (i.e., $\boldsymbol{s}_i$ is the i-th grid cell's spatial coordinates) and $\widehat{\bar{y}}^{l}_{GMB}$ is the l-th sample of AGB density for the AOI's PPD. We calculate lower and upper limits of a Bayesian 95% credible interval for $\widehat{\bar{y}}_{GMB}$ using the 2.5 and 97.5 percentiles, respectively, of the M $\widehat{\bar{y}}^{l}_{GMB}$ PPD samples. Note that this is not the only way to construct a 95% credible interval using PPD samples. For instance, a highest posterior density interval could be made using methods detailed in Turkkan and Pham-Gia (1993).

For a generic location $\boldsymbol{s}$, the spatial regression model is defined as

$$y(\boldsymbol{s}) = \beta_0 + \beta_1 x(\boldsymbol{s}) + w(\boldsymbol{s}) + \varepsilon(\boldsymbol{s}), \tag{11}$$

where $y(\boldsymbol{s})$ is AGB density, β_0 is the intercept coefficient, β_1 is the slope coefficient associated with CMS-AGB pixel value $x(\boldsymbol{s})$ and $w(\boldsymbol{s})$ is a spatial random effect. The term $\varepsilon(\boldsymbol{s})$ follows a normal distribution with mean zero and variance τ^2. Here, τ^2 is viewed as the measurement error variance. Like the MA estimator's assisting model (6), the parameters in (11) are estimated using all n^* observations within the study area.

Over the n^* observed locations, the spatial random effect $\boldsymbol{w} = (w(\boldsymbol{s}_1), w(\boldsymbol{s}_2), \ldots, w(\boldsymbol{s}_{n^*}))^T$ follows a multivariate normal distribution with a length n^*, zero mean vector and $n^* \times n^*$ covariance matrix Σ with $(i,j)^{th}$ element given by $C(\boldsymbol{s}_i, \boldsymbol{s}_j; \boldsymbol{\theta})$. For any two generic locations $\boldsymbol{s}$ and $\boldsymbol{s}'$ within the study region, the function used for $C(\boldsymbol{s}, \boldsymbol{s}'; \boldsymbol{\theta})$ must result in a symmetric and positive definite matrix Σ. Such functions are known as positive definite functions, details of which can be found in Cressie (1993), Chilès and Delfiner (2012), and Banerjee et al. (2014), among others. Here we specify $C(\boldsymbol{s}, \boldsymbol{s}'; \boldsymbol{\theta}) = \sigma^2\rho(\boldsymbol{s}, \boldsymbol{s}'; \phi)$, where $\boldsymbol{\theta} = \{\sigma^2, \phi\}$ and $\rho(\cdot; \phi)$ is a positive support correlation function with ϕ comprising one or more parameters that control the rate of correlation decay and smoothness of the process. The spatial process variance is given by σ^2, i.e., $\mathrm{Var}(w(\boldsymbol{s})) = \sigma^2$. This covariance function yields a *stationary* and *isotropic* process, i.e., a process with a constant variance and a correlation depending only on the Euclidean distance separating locations. The Mátern correlation function is a flexible class of correlation functions with desirable theoretical properties (Stein, 1999) and is given by

$$\rho(\|\boldsymbol{s} - \boldsymbol{s}^*\|; \phi) = \frac{1}{2^{\nu-1}\Gamma(\nu)}(\phi\|\boldsymbol{s} - \boldsymbol{s}'\|)^{\nu}\mathscr{K}_{\nu}(\|\boldsymbol{s} - \boldsymbol{s}'\|; \phi); \quad \phi > 0, \ \nu > 0, \tag{12}$$

where $\|\boldsymbol{s} - \boldsymbol{s}'\|$ is the Euclidean distance between $\boldsymbol{s}$ and $\boldsymbol{s}'$, $\phi = \{\phi, \nu\}$ with ϕ controlling the rate of correlation decay and ν controlling the process smoothness. The term Γ is the Gamma function and $\mathscr{K}_{\nu}$ is a modified Bessel function of the third kind with order ν. While it is theoretically ideal to estimate both ϕ and ν, it is often useful from a computational standpoint to fix ν and estimate only ϕ. For our current analysis, such a concession is reasonable given there is likely little information gain in estimating both parameters. Conveniently, when $\nu = 0.5$ the Mátern correlation reduces to the exponential correlation function, i.e., $\rho(\|\boldsymbol{s} - \boldsymbol{s}'\|; \phi) = \exp(-\phi\|\boldsymbol{s} - \boldsymbol{s}'\|)$. Therefore, only two process parameters are estimated $\boldsymbol{\theta} = \{\sigma^2, \phi\}$. To ease interpretation, we define the *effective spatial range* as the distance at which the correlation drops to 0.05 and present this in subsequent results.

Following Gelman et al. (2013) and Banerjee et al. (2014), given M MCMC samples from the joint posterior distribution of the posited model's parameters (i.e., β_0^l, β_1^l, τ^{2l}, $\boldsymbol{\theta}^l$ for $l = (1, 2, \ldots, M)$), composition sampling is used to sample one-for-one from the PPD vector $\widetilde{\boldsymbol{y}} = (\widetilde{y}(\boldsymbol{s}_1), \widetilde{y}(\boldsymbol{s}_2), \ldots, \widetilde{y}(\boldsymbol{s}_N))^T$. The specific form of this PPD is given in Finley and Banerjee (2020a, b).

3. Results and discussion

3.1. State-level estimates

Yearly state-level AGB density estimates derived using the four candidate estimators are shown in Fig. 1. It is evident from Fig. 1 that estimates garnered via the DR estimator are substantially different (higher) than the other three candidates at the state level. Fig. 1 also shows that estimates derived using the DB, MA, and GMB estimators are similar to each other. There is substantial overlap between the 95% uncertainty intervals for the DB, MA, and GMB estimates. Given that the DB estimator is known to be design-unbiased when probabilistically sampled data are used, we argue that the Oregon state-level DR estimator is likely biased. The MA and GMB estimators appear to be unbiased (since their estimates align well with the DB estimates) while still incorporating the CMS-AGB map predictions. We see that yearly 95%

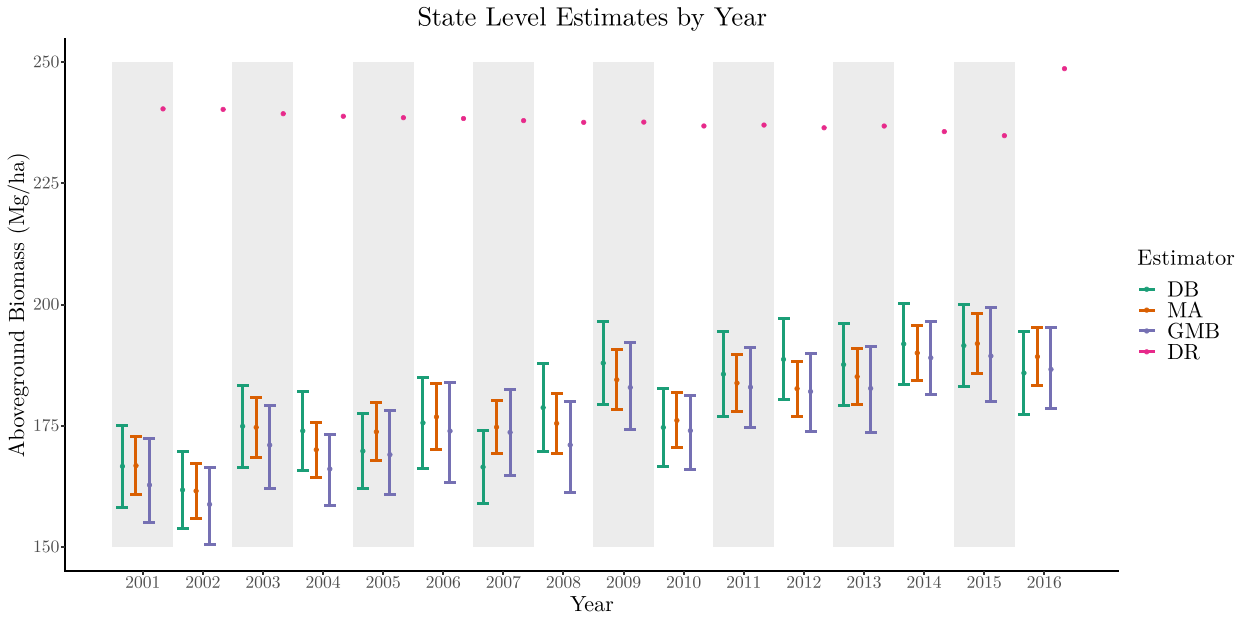

Fig. 1. State level AGB density estimates using the four candidate AGB estimators with associated 95% uncertainty intervals. The direct (DR), design-based (DB), model-assisted (MA) and geostatistical-model-based (GMB) estimators are shown in pink, green, orange and purple, respectively. (For interpretation of the references to colour in this figure legend, the reader is referred to the web version of this article.)

uncertainty intervals are narrower for the MA estimates than the DB estimates indicating that incorporating the CMS-AGB map product via the MA approach decreases estimation uncertainty, however we must be cautious making strong conclusions here as the MA estimator's variance estimator is negatively biased. The uncertainty interval widths for the GMB and DB estimates are similar. This suggests that even though the GMB approach incorporates the CMS-AGB map data, it does not necessarily result in increased estimation accuracy at the state level.

The DR estimates in Fig. 1 suggest that AGB density has remained largely constant between 2001 and 2015 with an apparent increase AGB density in 2016. However, the DB, MA and GMB estimators show a more gradual increase in AGB density between 2001 and 2016, similar to findings from the Oregon Department of Forestry (Christensen et al., 2019).

3.2. County-level estimates

Yearly estimates for Klamath, Clackamas and Benton counties are presented in Figs. 2, 3 and 4, respectively. We elected to showcase these three counties because they span the range of FIA plot sample sizes found in Oregon's counties (0 to ~90 plots per year). Figures for the remaining counties in Oregon are provided as supplementary materials.

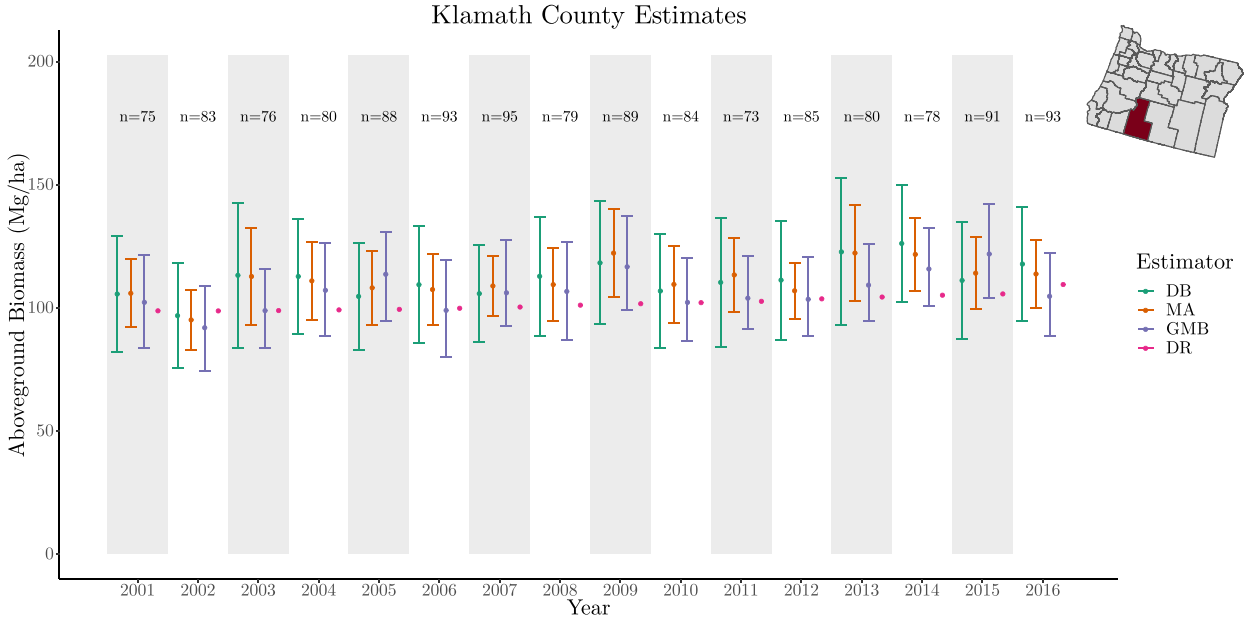

Fig. 2. Klamath County AGB density estimates using the four candidate AGB estimators with associated 95% uncertainty intervals. The direct (DR), design-based (DB), model-assisted (MA) and geostatistical-model-based (GMB) estimators are shown in pink, green, orange and purple, respectively. (For interpretation of the references to colour in this figure legend, the reader is referred to the web version of this article.)

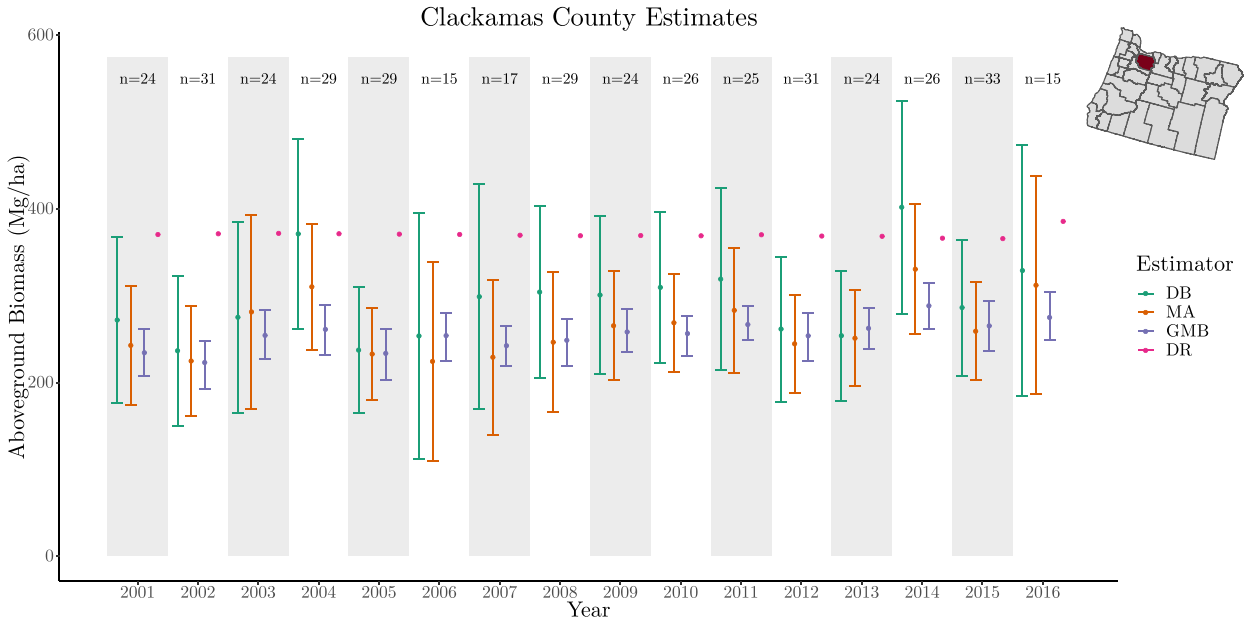

Fig. 3. Clackamas County AGB density estimates using the four candidate AGB estimators with associated 95% uncertainty intervals. The direct (DR), design-based (DB), model-assisted (MA) and geostatistical-model-based (GMB) estimators are shown in pink, green, orange and purple, respectively. (For interpretation of the references to colour in this figure legend, the reader is referred to the web version of this article.)

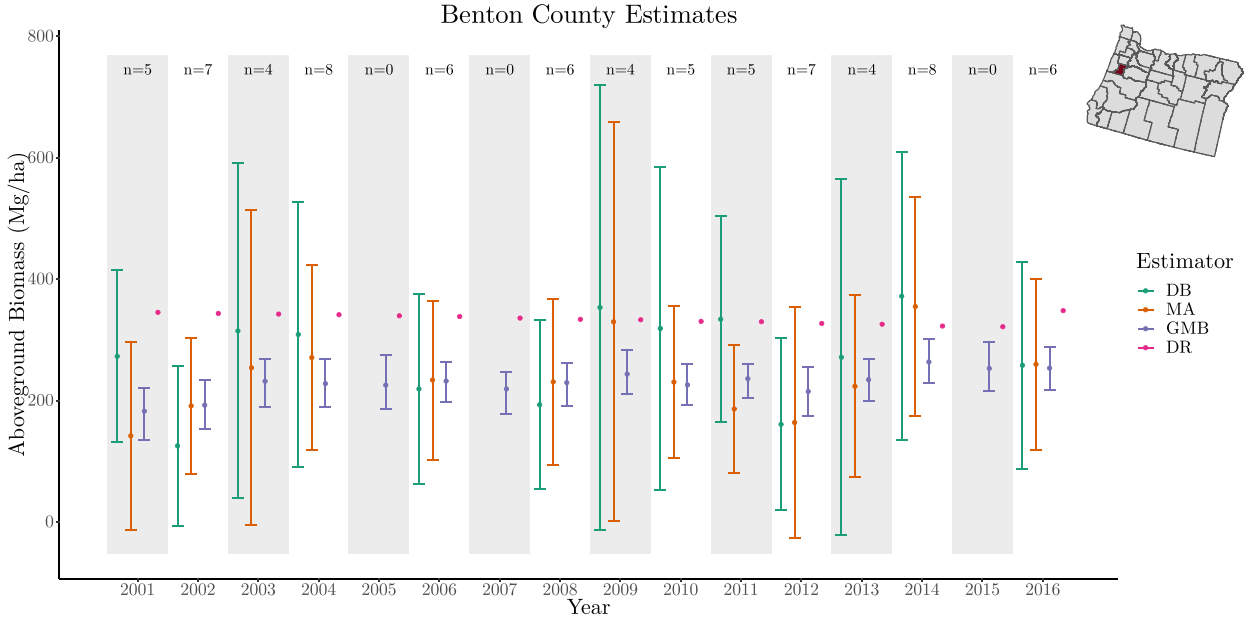

Fig. 4. Benton County AGB density estimates using the four candidate AGB estimators with associated 95% uncertainty intervals. The direct (DR), design-based (DB), model-assisted (MA) and geostatistical-model-based (GMB) estimators are shown in pink, green, orange and purple, respectively. (For interpretation of the references to colour in this figure legend, the reader is referred to the web version of this article.)

3.2.1. Klamath County (large sample size)

Klamath County has the highest number of field plots of the selected example counties (~84 plots per year). Fig. 2 shows uncertainty intervals for each candidate estimator in Klamath County. We see that the DB, MA and GMB estimator's 95% uncertainty intervals all overlap. It is also apparent that the MA and GMB estimator's uncertainty intervals are narrower than the DB estimator's uncertainty intervals for each year. This provides evidence that incorporating the CMS-AGB map in the MA and GMB estimators is leading to improved precision. In most years, the MA estimator's uncertainty intervals are narrower than the GMB estimator's uncertainty intervals. However, in 2003 and 2013, the GMB estimator is more precise than the MA estimator.

3.2.2. Clackamas County (moderate sample size)

Fig. 3 shows annual AGB density estimates and associated 95% uncertainty intervals using the four candidate estimators in Clackamas County. Field sample sizes in Clackamas County average ~23 plots per year. As in Klamath County (Fig. 2), the DB, MA and GMB estimator's 95% uncertainty intervals overlap in each year. The MA estimator's 95% uncertainty intervals are narrower than the DB estimator's intervals in all years except in 2003, indicating that the MA estimator tends to improve estimation precision through the inclusion of the CMS-AGB

map data. The GMB estimator's 95% uncertainty intervals are substantially narrower than the DB and MA intervals in each year. The ability of the GMB estimator to borrow information from proximate plot locations outside of Clackamas County in addition to its use of CMS-AGB map auxiliary data appears to lead to marked estimator precision improvement when compared to the DB and MA estimators in moderate sample size scenarios.

It is also apparent that the DB estimates are more variable than the MA and GMB estimates from year to year. For instance, the DB estimator's AGB density estimate shifts from ~275 Mg/ha in 2003 to nearly 375 Mg/ha in 2004 and, in 2005, drops to ~240 Mg/ha. This estimate volatility from year to year is likely caused by the lower field data sample sizes in Clackamas County. The additional information provided by the CMS-AGB map product appears to stabilize MA and GMB estimates year to year.

3.2.3. Benton County (small sample size)

Fig. 4 shows annual AGB density estimates and associated 95% uncertainty intervals using the four candidate estimators in Benton County. Sample sizes in Benton County are low with an average of ~5 field samples per year. No FIA field samples were available in 2005, 2007 and 2015. Due to the lack of field samples in those years, it is not possible to estimate AGB density using the DB and MA candidate estimators. However, the GMB estimator is a model-based approach which allows for estimation and uncertainty interval calculation in AOIs with no field data. We see that the GMB estimates in the years with no field data are similar to the GMB, MA and DB estimates in adjacent years. This suggests that even when no field data are available within the county, the GMB estimator is able to provide reasonable AGB density estimates by incorporating the CMS-AGB map predictions and borrowing field data information from outside the county via the spatial random effect $w(\boldsymbol{s})$.

The CMS-AGB map is improving estimate precision for Benton County, evidenced by the MA estimator's 95% uncertainty interval widths being narrower than the DB estimator's uncertainty interval widths in many years. It appears that both the DB and MA estimators may be adversely affected by the low FIA field sample sizes in Benton County, evidenced by large uncertainty interval widths. The GMB estimator provides substantially narrower 95% uncertainty intervals compared to the MA and DB estimator in all years considered. Similar to Clackamas County, the ability to borrow information from nearby plots outside of Benton County along with the added auxiliary information from the CMS-AGB map predictions leads to a precise GMB estimator.

3.2.4. County-level estimate assessment

Fig. 5 shows the relationship between AGB estimate 95% uncertainty interval width (95% uncertainty interval upper bound minus lower bound) and field sample size for the DB, MA and GMB estimators for all county-year combinations. We see that the MA and GMB estimators tend to produce estimates with narrower uncertainty intervals than the DB estimator for the within-county sample sizes encountered in this analysis. The GMB and MA estimators tend to produce similarly precise AGB estimates for county-years with $\geq$40 field plots. Estimator precision tends to decrease substantially as sample size decreases from 40 to 0 with the DB and MA estimators. It is well-known that DB estimators do not perform well when sample sizes become small (e.g., $\leq$30). Fig. 5 appears to corroborate this notion. We see that, at smaller sample sizes, the MA estimator does increase precision compared to the DB estimator through the incorporation of the CMS-AGB map. However, because the MA estimator falls within the DB statistical paradigm, we still see a dramatic decrease in precision as sample sizes drop below 30. The GMB estimator precision does not decrease as dramatically as the MA and DB estimators for sample sizes $\leq$30. The GMB estimator explicitly uses the spatial dependence structure in AGB density to weight information from proximate plots outside the AOI to help inform estimates within the AOI, leading to this increase in precision over the DB approach.

3.3. The HJ Andrews Experimental Forest

As mentioned throughout, a unique feature of the GMB estimator is that it can generate estimates and associated uncertainties in AOIs that contain no field plots. This feature makes it possible to calculate estimates and uncertainties for individual grid cells and map them. In this section, we explore this feature through an analysis in the HJA. Recall that the HJA is located in Lane County and has no FIA field plots within its borders. To explore the predictive performance of the GMB estimator in the HJA in the year 2016, we produce AGB density estimates and

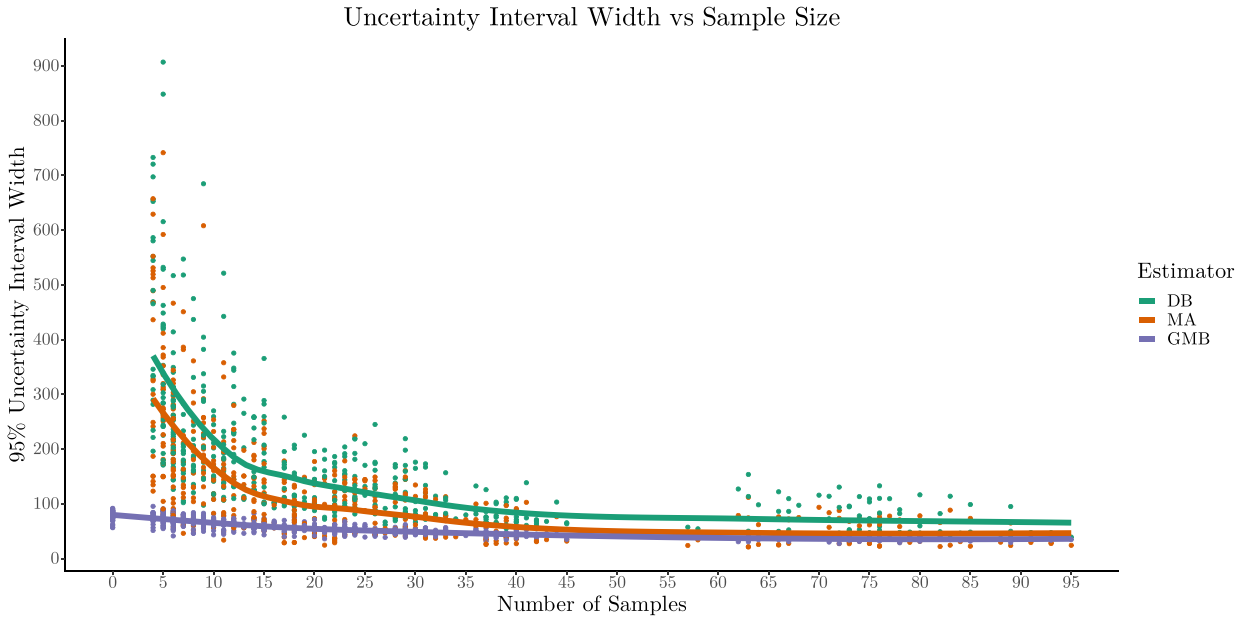

Fig. 5. A scatterplot showing the relationship between 95% uncertainty interval width (upper bound minus lower bound) versus the number FIA field samples for the design-based (DB), model-assisted (MA) and geostatistical-model-based (GMB) estimators. Trend lines represent the moving average for 95% uncertainty interval width.

posterior standard deviations for a variety of pixel resolutions within the HJA, for forest stands within the HJA and for variety of different sized concentric circles at the center of the HJA. We selected the year 2016 for the HJA analysis because it was the most current CMS-AGB map available.

We first examine pixel-level predictions within the HJA. Figs. 6 and 7 display grid cell-level AGB estimates and associated posterior standard deviations for the HJA at varying spatial resolutions, respectively. These resolutions span from 30 m pixels to 240 m pixels. In Fig. 6, we see how the GMB estimator's AGB estimates vary across the HJA and can even identify potential areas where harvests have taken place (see, e.g., the South Eastern corner of the HJA). Generally the GMB estimator produces similar maps at each pixel size, with more details visible at finer resolutions. Further, in Fig. 7 we see relatively constant uncertainty across pixels for each pixel-level resolution within the HJA. For 30 m pixels, we see very high levels of uncertainty, but for 90 m, 180 m, and 240 m pixels we see a significant drop in uncertainty as pixel size increases. We note that for 30 m pixels, posterior standard deviations in the HJA average ~100 Mg/ha, indicating that one should use caution when using this map to determine 30 m grid cell-level AGB stocking or making other management decisions at the grid cell level.

Fig. 8 shows a map of forest stands in the HJA and Table 1 shows their corresponding AGB density estimates and uncertainties. We see in Table 1 that generally, as forest stand area increases there is a decrease in the posterior standard deviation. We see that the coefficient of variation for forest stands hovers around 0.1, leading us to believe that this case study in the HJA provides evidence that the GMB estimator may be useful for conducting stand-level carbon accounting even when there is no field data available within the stand.

We also examine predictive performance through the use of a set of concentric circles of varying size to use as our AOIs. Note that Fig. 8 shows the geographic center of the HJA (the center of these circles). Fig. 9 displays the posterior standard deviations for each concentric circle as areal extent of the circle increases. Notably, we see that as the AOI's areal extent increases there is a decrease in the posterior standard deviation. Starting at the smallest circle areal extent of 0.09 ha the posterior standard deviation drastically decreases until the circles are approximately 2 ha, and then the trend levels out. This gives us a good sense of what sized AOIs the GMB estimator can provide sufficient precision for meaningful inference, given that there are no field plots within the AOI.

3.4. Geostatistical model-based prediction accuracy, bias and uncertainty interval coverage

In this section, we explore the accuracy, bias and uncertainty interval coverage of the GMB and CMS-AGB fitted values and predictions at the FIA plot level. Ideally, we would have assessed accuracy, bias and uncertainty interval coverage for areal estimates (e.g., county-level estimates). This is not possible however since we do not have AGB observations that can be safely considered true values for areal extents larger than the FIA plot. Specifically, we examine GMB model fitted values and 10-fold holdout predictions with associated 95% credible intervals for each year (i.e., 2001–2016). GMB fitted values and associated 95% credible intervals were generated using PPDs sampled at FIA plot locations with the full GMB model (i.e., no FIA observations held out during model fitting). To generate GMB 10-fold holdout predictions and 95% credible intervals, FIA observations were randomly split into ten subsets. Then a GMB model was fit with nine subsets and used to generate PPDs for the held out subset. This process was repeated ten times, holding out a different subset each time. The Root Mean Squared Error (RMSE) statistic was used to estimate accuracy. 95% coverage probability was estimated as the proportion of 95% credible intervals that contained the associated FIA plot value. Results of this analysis are shown in Table 2. Fig. 10 shows combined CMS-AGB map, GMB fitted values and GMB 10-fold holdout predicted values versus FIA plot observations. Similar figures for individual years are provided as supplementary materials.

GMB fitted values and holdout predictions are more accurate than the CMS-AGB map predictions. Table 2 shows that GMB fitted values and holdout prediction RMSE metrics are substantially lower than the CMS-AGB map RMSE metrics for every year considered. The level of improvement varies slightly from year-to-year, but GMB holdout prediction RMSE combined across model years shows a 25% improvement in prediction accuracy compared to the CMS-AGB maps. Table 2 also shows that GMB fitted values and holdout predictions are substantially less bias than the CMS-AGB map predictions. GMB fitted values and holdout prediction bias is slightly negative, but near zero (−0.56 Mg/ha, −0.45 Mg/ha), whereas CMS-AGB map bias is near 60 Mg/ha. Coverage probability of GMB fitted values combined across model years is estimated at 0.95. Coverage probability of GMB holdout predictions is estimated at 0.93. With estimated coverage probabilities being nearly ideal (target value is 0.95), we argue that the GMB modeling approach

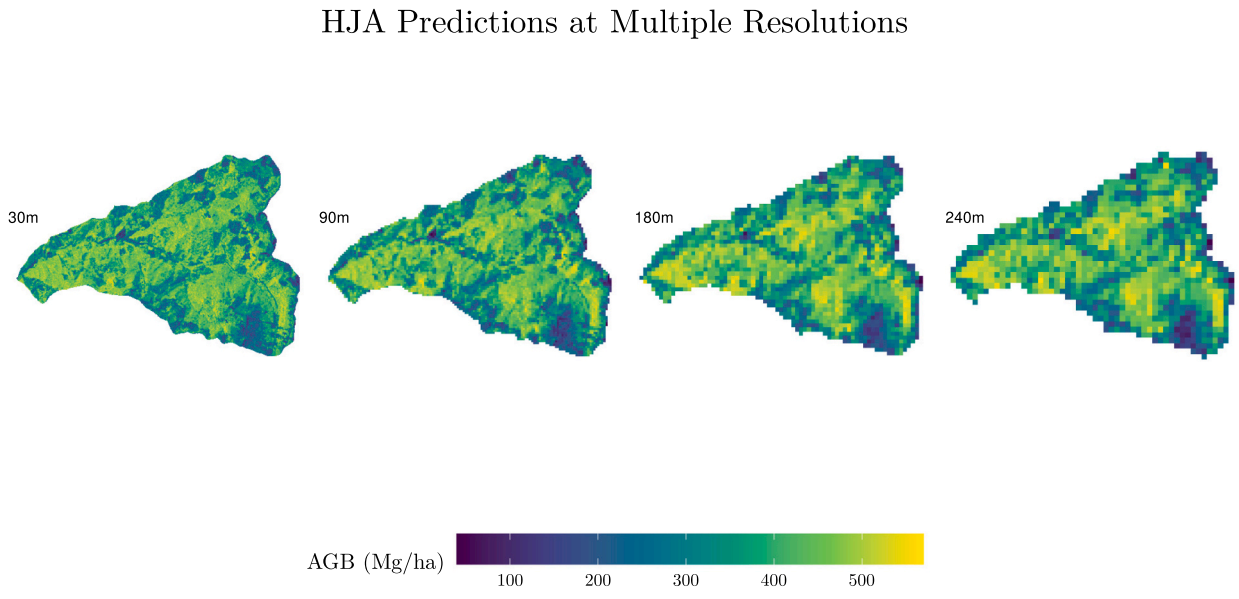

Fig. 6. Grid cell-level AGB density estimates at HJ Andrews Experimental Forest generated using the geostatistical-model-based (GMB) estimator.

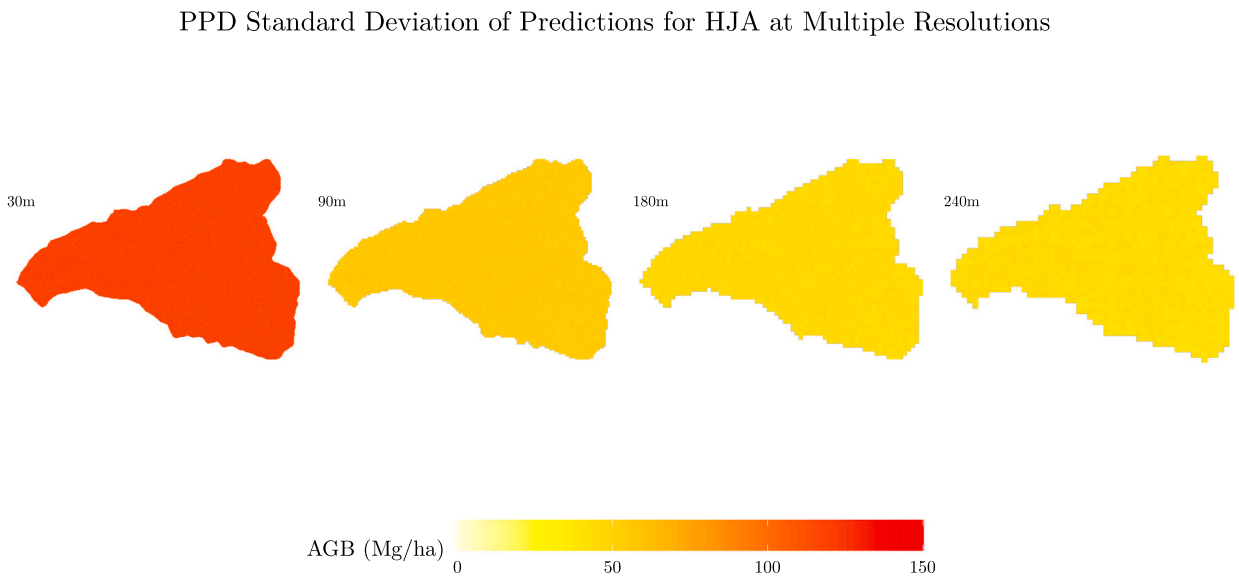

Fig. 7. Grid cell-level AGB density posterior standard deviations at HJ Andrews Experimental Forest using the geostatistical-model-based (GMB) estimator.

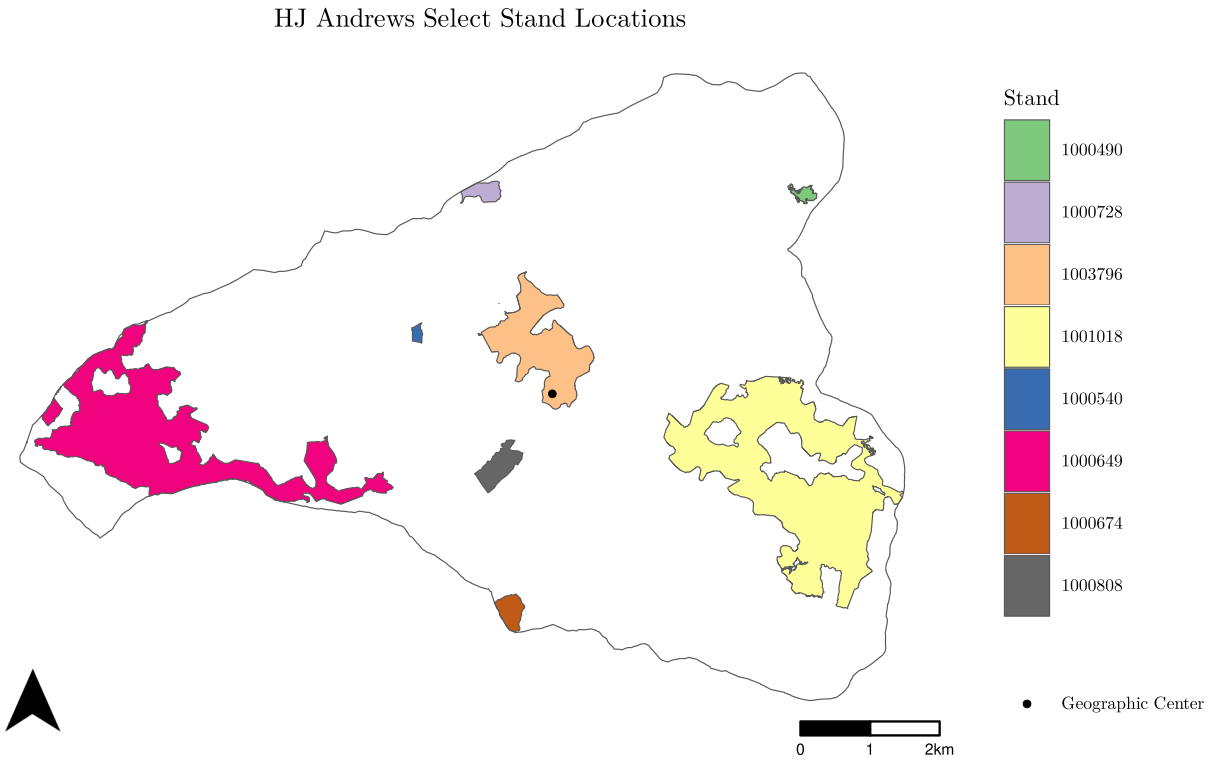

Fig. 8. Selected Stand Locations for the HJ Andrews Experimental Forest.

adequately characterizes uncertainty with statistical rigor.

4. Conclusion

We examined an MA and GMB estimator that leveraged an ML-produced CMS-AGB map product to estimate AGB density. We compared the two estimators to a DR estimator that used only the CMS-AGB map predictions and to a DB estimator that used only probabilistically sampled FIA field data. Comparing these four estimators provided evidence that the DR estimator is likely biased and that the MA and GMB estimators appeared to correct for bias induced by the CMS-AGB map predictions through the incorporation of FIA field data. The MA- and GMB-derived AGB density estimates did not substantially differ from the DB estimates for AOIs where the DB estimates of AGB density had sufficient precision.

Incorporating the CMS-AGB map at the state level resulted in a moderate increase in estimation precision when the MA estimator was used, however some of this gain in precision may be due to the negative bias of the variance estimator for the MA estimator. When examining the GMB estimator at the state level we found it to appear less biased than the DR estimator, however it did not result in increased precision over the DB estimator. MA- and GMB-derived estimates of AGB density for counties with large field sample sizes saw marginal gains in precision compared to the DB estimator. The GMB estimator's precision was

Table 1
Aboveground biomass (AGB) density (Mg/ha) estimates with associated 95% uncertainty intervals for HJ Andrews Experimental Forest and stands within. Posterior predictive distribution standard deviations (PPD SD) and stand areas are also presented.

Stand ID	AGB Density (Mg/ha)	PPD SD (Mg/ha)	Area (Ha)
1000728	326.01 (232.96, 411.09)	46.76	3
1000490	374.78 (298.37, 462.05)	42.40	6
1000540	298.41 (221.15, 377.76)	42.24	12
1001018	262.92 (172.34, 340.12)	42.47	15
1003796	314.22 (236.53, 404.35)	42.43	23
1000649	445.97 (365.42, 536.51)	41.16	130
1000808	455.71 (378.68, 533.48)	38.65	418
100674	428.95 (348.38, 499.78)	38.36	459
HJ Andrews	392.72 (319.58, 454.04)	32.51	6400

markedly better than the MA and DB estimators for AOIs with moderate to small sample sizes. The GMB estimator tended to be the most precise estimator when the AOI's sample sizes dropped below 30. We also examined the influence of AOI size on the GMB estimator's uncertainty metrics when there were no field plots within the AOI by looking at concentric circles of varying size within the HJA. We saw that uncertainty was very high for AOIs of less than 1 ha, moderate for AOIs of area 1–2 ha, and sufficient for areas over 2 ha. This result suggests that the GMB estimator may be useful for forest stand-level AGB density estimation when no plots are available within the AOI due to its ability to borrow strength from proximate field data outside the stand. We also examined the accuracy and coverage probability of plot-level AGB predictions using the GMB estimator. We saw the the GMB estimator had an overall prediction accuracy improvement of nearly 25% compared to the CMS-AGB map at the FIA plot level. We also observed that GMB 95% coverage probabilities were sufficient to say that the GMB estimator adequately characterizes uncertainty with statistical rigor at the FIA plot level.

Perturbed FIA plot coordinates were used in this analysis meaning that plot locations were potentially off by a kilometer or more. The DB and MA estimators examined here do not explicitly depend on spatial location information. Because of this, the DB and MA estimators are not adversely affected by plot perturbing (as long as the AGB map predictions are extracted for FIA plots before perturbing, as was done in this

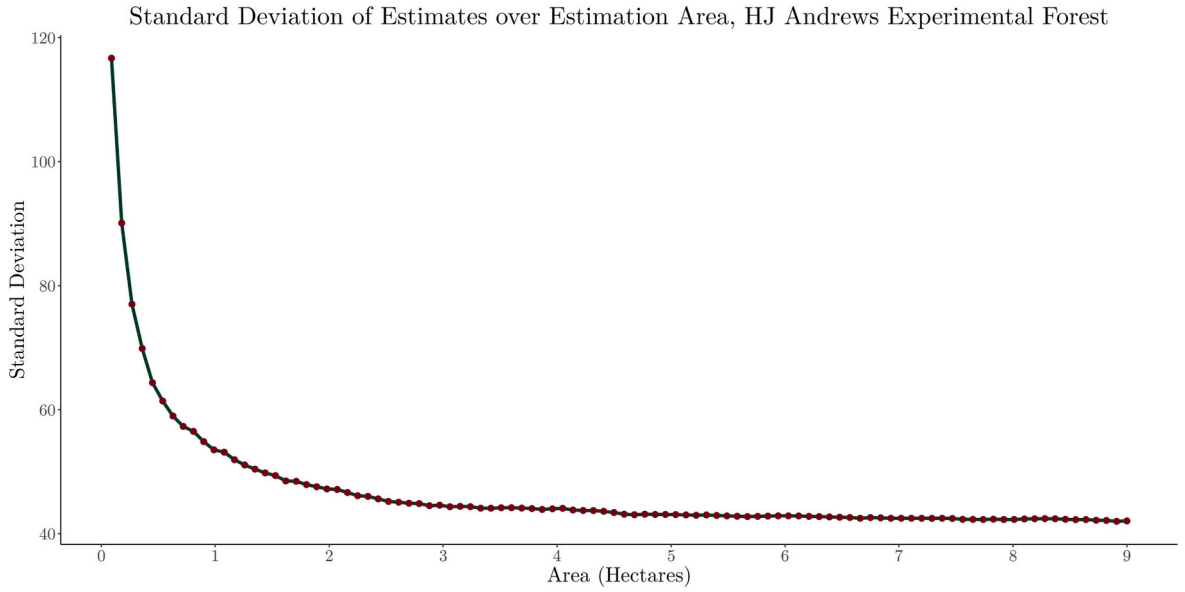

Fig. 9. Posterior standard deviations for concentric circular AOIs centered at the geographic center of HJ Andrews Experimental Forest.

Table 2
Geostatistical model-based and CMS-AGB map accuracy, bias and 95% uncertainty interval coverage probability (CP). Accuracy is assessed using the root mean squared error (RMSE) statistic.

	GMB Model Fitted Values			GMB 10-Fold Holdout Prediction			CMS-AGB Map		
Year	95% CP	RMSE	BIAS	95% CP	RMSE	BIAS	95% CP	RMSE	BIAS
2001	0.93	106.61	−0.52	0.93	112.54	−0.73	–	166.26	73.49
2002	0.95	97.95	−0.64	0.93	112.09	−0.57	–	166.64	78.88
2003	0.99	64.11	−0.23	0.94	120.56	−0.50	–	162.59	64.86
2004	0.96	90.14	−0.38	0.93	112.78	−0.67	–	165.98	72.04
2005	0.95	110.83	−0.61	0.94	120.69	0.08	–	167.52	61.01
2006	0.96	121.30	−0.99	0.94	130.83	−0.31	–	166.26	60.77
2007	0.94	107.20	−0.74	0.93	113.10	−0.20	–	156.51	55.73
2008	0.94	108.10	−0.28	0.93	118.02	−0.73	–	156.35	64.09
2009	0.94	121.09	−0.53	0.93	128.20	−0.69	–	161.53	55.42
2010	0.94	103.33	−0.92	0.93	112.61	−0.66	–	150.16	59.73
2011	0.94	105.00	−0.69	0.93	111.90	−0.53	–	147.93	54.40
2012	0.95	98.08	−0.02	0.93	115.73	−0.68	–	149.89	57.42
2013	0.97	88.19	−0.57	0.94	115.00	−0.07	–	149.06	53.24
2014	0.98	62.36	−0.35	0.94	112.56	−0.31	–	145.76	46.82
2015	0.95	117.11	−0.66	0.93	125.61	−0.23	–	153.19	42.62
2016	0.95	106.59	−0.90	0.94	120.16	−0.51	–	149.02	57.54
Combined	0.95	101.90	−0.56	0.93	117.85	−0.45	–	157.14	59.74

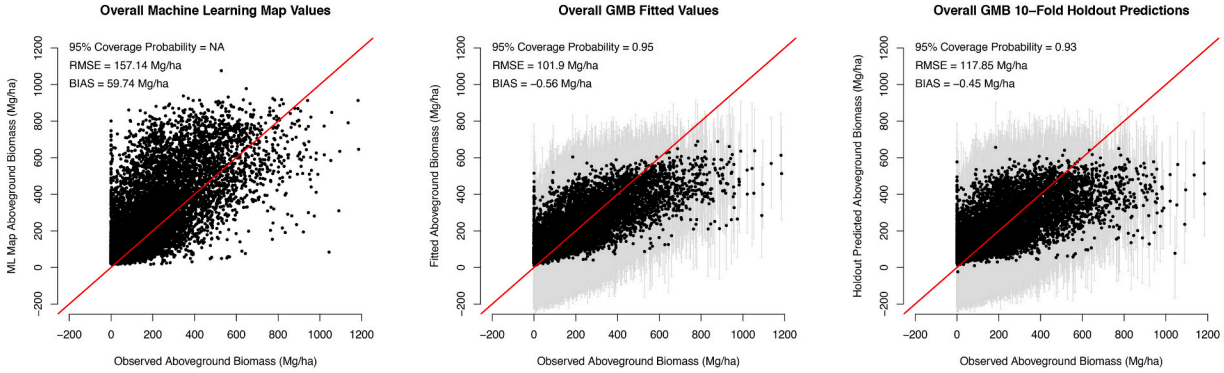

(a) CMS-AGB values versus FIA plot AGB observations

(b) Fitted GMB values versus FIA plot AGB observations

(c) 10-Fold Holdout GMB Predictions versus FIA plot AGB observations

Fig. 10. Combined prediction accuracy and uncertainty interval coverage for GMB models. Grey vertical bars show the 95% uncertainty interval produced at the FIA plot location. Red line is the one-to-one line. (For interpretation of the references to colour in this figure legend, the reader is referred to the web version of this article.)

study). However, the GMB estimator incorporates a spatial random effect that explicitly models AGB spatial dependence based on intersite distances between plot locations. Using perturbed plot locations in the GMB estimator likely inhibits the estimators ability to model spatial autocorrelation precisely. We see in Table 3 that effective range estimates vary substantially from year to year. We also see that effective range uncertainty interval widths are very high, indicating that the GMB estimator was not able to estimate how far-reaching the spatial correlation structure was between plots with a high degree of certainty.

In future work, we plan to examine the GMB estimator more thoroughly for this application using true FIA plot coordinate locations. Additionally, we plan to test how the GMB estimator performs when FIA subplot-level observations are used for model fitting. We believe that adapting the GMB estimator in this way may improve precision by allowing for the model to more precisely estimate the spatial autocorrelation structure in the data. We also plan to extend the GMB estimator to account for model nonstationarity by incorporating spatially varying coefficients (Babcock et al., 2015). It is likely that the relationship between FIA plot observations and the CMS-AGB map product is not the same across Oregon given how the CMS-AGB map was generated (it likely over-represents some forest areas and under-represent others). Allowing the GMB estimator's model coefficients to vary across space may account for issues with local model lack-of-fit and lead to improved AGB density estimation. We also plan to begin exploring spatio-temporal extensions to the GMB framework to allow for AGB change estimation.

This work showcases two approaches capable of incorporating ML-produced predictions of AGB to improve AGB density estimation precision for a variety of AOIs. We see that it is possible to estimate AGB density for AOIs within a design- and model-based statistical paradigm and generate statistically defensible uncertainty characterizations when the assumptions underpinning the approaches are sufficiently met. The estimators explored here have the potential to vastly improve our ability to estimate forest biomass in a way that is useful to carbon trading markets. Being able to provide statistically rigorous uncertainty metrics alongside estimates allows carbon trading markets to incorporate these metrics into their accounting procedures. By incorporating auxiliary remote sensing-driven forest biomass maps using the approaches examined here, we can decrease costs associated with forest carbon accounting by reducing the amount field data needed to produce sufficiently precise estimates. Adopting these approaches to estimation can incentivize small forest landowners to enroll in carbon trading programs by reducing barriers to entry.

CRediT authorship contribution statement

Ethan Emick: Conceptualization, Methodology, Formal analysis, Writing – original draft, Writing – review & editing, Investigation. **Chad Babcock:** Conceptualization, Methodology, Formal analysis, Writing – original draft, Writing – review & editing, Funding acquisition. **Grayson W. White:** Methodology, Writing – original draft, Writing – review & editing. **Andrew T. Hudak:** Conceptualization, Writing – original draft, Funding acquisition. **Grant M. Domke:** Conceptualization,

Table 3
Geostatistical-model-based (GMB) parameter and state-level aboveground biomass (AGB) density (Mg/ha) estimates with associated 95% credible intervals. Effective range is the distance in kilometers where the spatial correlation between locations drops to 0.05.

Year	β_0	β_1	σ^2	τ^2	Effective Range (km)	AGB density (Mg/ha)
2001	25.30 (−1.99, 46.69)	0.56 (0.51, 0.61)	1063.97 (483.12, 2099.72)	11,976.19 (10,640.90, 13,305.16)	175.92 (45.58, 602.41)	163.00 (154.03, 172.23)
2002	23.27 (7.72, 38.68)	0.56 (0.52, 0.61)	1919.84 (681.74, 4625.29)	10,827.60 (8569.42, 12,410.26)	50.59 (22.16, 141.97)	159.54 (150.95, 167.38)
2003	35.33 (20.32, 49.89)	0.56 (0.52, 0.61)	6746.55 (1639.38, 11,753.57)	7919.18 (3437.03, 12,960.22)	14.00 (10.39, 56.43)	171.85 (161.60, 180.80)
2004	31.65 (11.05, 48.14)	0.56 (0.41, 0.61)	2385.57 (899.19, 6323.34)	10,682.34 (6983.40, 12,732.48)	52.81 (19.52, 206.27)	166.61 (157.73, 174.89)
2005	40.22 (13.61, 58.32)	0.53 (0.49, 0.59)	1448.05 (661.72, 2826.32)	13,420.53 (11,947.91, 14,972.43)	125.78 (55.38, 315.18)	170.51 (161.25, 179.01)
2006	24.03 (−3.70, 42.59)	0.62 (0.57, 0.67)	999.31 (354.68, 2420.21)	16,055.77 (14,053.96, 18,259.09)	62.62 (16.70, 715.75)	174.69 (164.58, 185.02)
2007	47.28 (24.09, 61.89)	0.53 (0.48, 0.57)	775.98 (316.81, 2269.16)	11,994.16 (10,442.51, 13,571.97)	40.44 (12.15, 887.06)	173.77 (166.24, 182.43)
2008	19.77 (−3.67, 40.92)	0.63 (0.58, 0.67)	1278.70 (585.05, 2647.26)	12,796.94 (11,321.22, 14,471.53)	107.34 (40.75, 437.71)	170.76 (160.96, 179.74)
2009	32.92 (6.63, 53.13)	0.61 (0.56, 0.66)	950.91 (427.07, 2074.20)	15,651.23 (13,933.58, 17,421.14)	146.03 (25.31, 851.85)	183.23 (173.12, 192.67)
2010	34.07 (19.51, 48.24)	0.59 (0.54, 0.63)	1134.40 (441.25, 2852.70)	11,607.07 (9784.78, 13,138.17)	44.95 (17.03, 145.59)	174.60 (166.03, 183.08)
2011	38.70 (24.63, 52.04)	0.60 (0.56, 0.65)	1068.37 (373.33, 4130.61)	11,363.71 (8436.50, 13,014.75)	16.33 (10.14, 392.13)	183.05 (175.29, 191.92)
2012	32.61 (17.60, 46.10)	0.63 (0.59, 0.67)	1985.78 (675.95, 5828.67)	11,355.93 (7737.36, 13,327.71)	37.37 (12.71, 103.10)	182.36 (174.30, 190.50)
2013	38.19 (23.63, 51.15)	0.61 (0.56, 0.65)	3312.29 (682.79, 9285.90)	11,041.76 (4450.04, 13,120.83)	17.62 (10.05, 150.72)	182.67 (174.13, 191.83)
2014	41.59 (27.51, 56.12)	0.62 (0.58, 0.67)	5264.44 (1630.35, 9526.22)	10,041.76 (3565.31, 11,260.74)	19.11 (12.00, 40.48)	189.77 (181.48, 197.82)
2015	39.40 (7.87, 60.04)	0.62 (0.57, 0.67)	1237.48 (495.66, 2702.19)	14,886.90 (13,381.16, 16,516.42)	115.61 (45.27, 678.78)	189.69 (180.54, 199.27)
2016	26.34 (9.98, 41.53)	0.64 (0.59, 0.69)	1582.37 (579.49, 4883.16)	12,488.88 (9296.08, 14,286.75)	42.75 (10.37, 112.60)	187.13 (178.75, 197.51)

Methodology, Funding acquisition. **Andrew O. Finley:** Conceptualization, Formal analysis, Software, Writing – review & editing.

Declaration of Competing Interest

The authors declare that they have no known competing financial interests or personal relationships that could have appeared to influence the work reported in this paper.

Data availability

Data will be made available on request.

Acknowledgments

This work was supported, in part, by the USDA Forest Service Forest Inventory and Analysis (FIA) and Forest Health Monitoring (FHM) programs, and National Aeronautics and Space Administration's Carbon Monitoring System Program. The first author's work was also supported through the Minnesota Agricultural Research, Education and Extension Tech Transfer program (AGREETT). The third author received additional support from the National Science Foundation (NSF) NSF/EF 1253225 and NSF/DMS 1916395. Data were provided by the H.J. Andrews Experimental Forest and Long Term Ecological Research (LTER) program, administered cooperatively by Oregon State University, the USDA Forest Service Pacific Northwest Research Station, and the Willamette National Forest. This material is based upon work supported by the National Science Foundation under the grant LTER8 DEB-2025755.

Appendix A. Supplementary data

Supplementary data to this article can be found online at https://doi.org/10.1016/j.rse.2023.113678.

References

Babcock, C., Finley, A.O., Bradford, J.B., Kolka, R., Birdsey, R., Ryan, M.G., 2015. LiDAR based prediction of forest biomass using hierarchical models with spatially varying coefficients. Remote Sens. Environ. 169, 113–127.

Babcock, C., Finley, A.O., Andersen, H.E., Pattison, R., Cook, B.D., Morton, D.C., Alonzo, M., Nelson, R., Gregoire, T., Ene, L., Gobakken, T., Næsset, E., 2018. Geostatistical estimation of forest biomass in interior Alaska combining landsat-derived tree cover, sampled airborne lidar and field observations. Remote Sens. Environ. 212, 212–230.

Ball, T.M., Squeglia, L.M., Tapert, S.F., Paulus, M.P., 2020. Double dipping in machine learning: problems and solutions. Biol. Psychiatry. Cogn. Neurosc. Neuroimag. 5, 261.

Banerjee, S., Carlin, B., Gelfand, A., 2014. Hierarchical moDeling and anAlysis for Spatial Data, Second edition. Chapman & Hall/CRC Monographs on Statistics & Applied Probability, Taylor & Francis.

Bansal, S., Brodie, L., Stanton, S., Waddell, K., Palmer, M., Christensen, G., Kuegler, O., Chase, J., Thompson, J., Jovan, S., Gray, A., Todd, M., 2017. Oregon's forest resources, 2001–2010: ten-year forest inventory and analysis report. *Gen. Tech. Rep. PNW-GTR-958. Portland, OR: U.S. Department of Agriculture, Forest Service, Pacific Northwest Research Station. 130 p.*, 958.

Bechtold, W.A., Patterson, P.L., 2005. The Enhanced Forest Inventory and Analysis Program: National Sampling Design and Estimation Procedures. US Department of Agriculture Forest Service, Southern Research Station Asheville, North Carolina.

Blackard, J., Finco, M., Helmer, E., Holden, G., Hoppus, M., Jacobs, D., Lister, A., Moisen, G., Nelson, M., Riemann, R., Ruefenacht, B., Salajanu, D., Weyermann, D., Winterberger, K., Brandeis, T., Czaplewski, R., McRoberts, R., Patterson, P., Tymcio, R., 2008. Mapping U.S. forest biomass using nationwide forest inventory data and moderate resolution information. Remote Sens. Environ. 112, 1658–1677. Remote Sensing Data Assimilation Special Issue.

Breiman, L., 2001. Random forests. Mach. Learn. *45 (1). 2001.* 45, 5–32.

Cassel, C.M., Sarndal, C.E., Wretman, J.H., 1976. Some results on generalized difference estimation and generalized regression estimation for finite populations. Biometrika 63, 615–620. http://www.jstor.org/stable/2335742.

Chen, L., Ren, C., Zhang, B., Wang, Z., Xi, Y., 2018. Estimation of forest above-ground biomass by geographically weighted regression and machine learning with sentinel imagery. Forests 9, 582.

Chilès, J., Delfiner, P., 2012. Geostatistics: Modeling Spatial Uncertainty. Wiley Series in Probability and Statistics. Wiley.

Christensen, G.A., Gray, A.N., Kuegler, O., Yost, A.C., 2019. Oregon Forest Ecosystem Carbon Inventory: 2001–2016.

Cressie, N.A.C., 1993. Statistics for Spatial Data. Wiley.

Duncanson, L., Armston, J., Disney, M., Avitabile, V., Barbier, N., Calders, K., Carter, S., Chave, J., Herold, M., Crowther, T.W., et al., 2019. The importance of consistent global forest aboveground biomass product validation. Surv. Geophys. 40, 979–999.

Duncanson, L., Kellner, J.R., Armston, J., Dubayah, R., Minor, D.M., Hancock, S., Healey, S.P., Patterson, P.L., Saarela, S., Marselis, S., Silva, C.E., Bruening, J., Goetz, S.J., Tang, H., Hofton, M., Blair, B., Luthcke, S., Fatoyinbo, L., Abernethy, K., Alonso, A., Andersen, H.E., Aplin, P., Baker, T.R., Barbier, N., Bastin, J.F., Biber, P., Boeckx, P., Bogaert, J., Boschetti, L., Boucher, P.B., Boyd, D.S., Burslem, D.F., Calvo-Rodriguez, S., Chave, J., Chazdon, R.L., Clark, D.B., Clark, D.A., Cohen, W.B., Coomes, D.A., Corona, P., Cushman, K.C., Cutler, M.E., Dalling, J.W., Dalponte, M., Dash, J., de Miguel, S., Deng, S., Ellis, P.W., Erasmus, B., Fekety, P.A., Fernandez-Landa, A., Ferraz, A., Fischer, R., Fisher, A.G., García-Abril, A., Gobakken, T., Hacker, J.M., Heurich, M., Hill, R.A., Hopkinson, C., Huang, H., Hubbell, S.P., Hudak, A.T., Huth, A., Imbach, B., Jeffery, K.J., Katoh, M., Kearsley, E., Kenfack, D., Kljun, N., Knapp, N., Kráel, K., Krůček, M., Labrière, N., Lewis, S.L., Longo, M., Lucas, R.M., Main, R., Manzanera, J.A., Martínez, R.V., Mathieu, R., Memiaghe, H., Meyer, V., Mendoza, A.M., Monerris, A., Montesano, P., Morsdorf, F., Næsset, E., Naidoo, L., Nilus, R., O'Brien, M., Orwig, D.A., Papathanassiou, K., Parker, G., Philipson, C., Phillips, O.L., Pisek, J., Poulsen, J.R., Pretzsch, H., Rüdiger, C., Saatchi, S., Sanchez-Azofeifa, A., Sanchez-Lopez, N., Scholes, R., Silva, C.A., Simard, M., Skidmore, A., Stereńczak, K., Tanase, M., Torresan, C., Valbuena, R., Verbeeck, H., Vrska, T., Wessels, K., White, J.C., White, L.J., Zahabu, E., Zgraggen, C., 2022. Aboveground biomass density models for nasa's global ecosystem dynamics investigation (gedi) lidar mission. Remote Sens. Environ. 270, 112845.

Ekström, M., Nilsson, M., 2021. A comparison of model-assisted estimators, with and without data-driven transformations of auxiliary variables, with application to forest inventory. Front. Forests Global Change 4. https://doi.org/10.3389/ffgc.2021.764495.

Fekety, P., Hudak, A., 2019. Annual Aboveground Biomass Maps for Forests in the Northwestern USA, 2000-2016. ORNL Distributed Active Archive Center, 10.334/ORNLDAAC/1766.

Fekety, P.A., Hudak, A.T., Bright, B., 2020. Tree and Stand Attributes for a Carbon Monitoring System for Mapping Regional, Annual Aboveground Biomass across the Northwestern Usa. Forest Service Research Data Archive, Fort Collins CO. https://doi.org/10.2737/RDS-2020-0026.

Finley, A., Banerjee, S., 2020a. spBayes: Univariate and Multivariate Spatial-Temporal Modeling. https://cran.r-project.org/package=spBayes r package version 0.4–3.

Finley, A.O., Banerjee, S., 2020b. Bayesian spatially varying coefficient models in the spbayes r package. Environ. Model. Softw. 125, 104608.

Finley, A.O., Banerjee, S., MacFarlane, D.W., 2011. A hierarchical model for quantifying forest variables over large heterogeneous landscapes with uncertain forest areas. J. Am. Stat. Assoc. 106, 31–48. https://doi.org/10.1198/jasa.2011.ap09653 pMID: 26139950.

Finley, A.O., Banerjee, S., Cook, B.D., Bradford, J.B., 2013. Hierarchical bayesian spatial models for predicting multiple forest variables using waveform lidar, hyperspectral imagery, and large inventory datasets. Int. J. Appl. Earth Obs. Geoinf. 22, 147–160.

Franklin, J., Logan, T.L., Woodcock, C.E., Strahler, A.H., 1986. Coniferous forest classification and inventory using landsat and digital terrain data. IEEE Trans. Geosci. Remote Sens. GE-24, 139–149.

Frescino, T.S., McConville, K.S., White, G.W., Toney, J.C., Moisen, G.G., 2022. Small area estimates for national applications: a database to dashboard strategy using fiesta. Front. Forests Global Change 5. https://doi.org/10.3389/ffgc.2022.779446.

Gelfand, A.E., Kim, H.J., Sirmans, C.F., Banerjee, S., 2003. Spatial modeling with spatially varying coefficient processes. J. Am. Stat. Assoc. 98, 387–396.

Gelman, A., Carlin, J., Stern, H., Dunson, D., Vehtari, A., Rubin, D., 2013. Bayesian Data Analysis, Third edition. Chapman & Hall/CRC Texts in Statistical Science, Taylor & Francis.

Gregoire, T.G., 1998. Design-based and model-based inference in survey sampling: appreciating the difference. Can. J. For. Res. 28, 1429–1447.

Gregoire, T.G., Ståhl, G., Næsset, E., Gobakken, T., Nelson, R., Holm, S., 2011. Model-assisted estimation of biomass in a lidar sample survey in Hedmark county, Norway. Can. J. For. Res. 41, 83–95.

Hall, R.J., Skakun, R.S., Arsenault, E.J., Case, B.S., 2006. Modeling forest stand structure attributes using landsat etm+ data: application to mapping of aboveground biomass and stand volume. For. Ecol. Manag. 225, 378–390.

Hastie, T., Tibshirani, R., Friedman, J., 2009. The Elements of Statistical Learning. Springer, New York.

Houghton, R.A., Hall, F., Goetz, S.J., 2009. Importance of biomass in the global carbon cycle. J. Geophys. Res. Biogeosci. 114.

Huang, W., Dolan, K., Swatantran, A., Johnson, K., Tang, H., O'Neil-Dunne, J., Dubayah, R., Hurtt, G., 2019. High-resolution mapping of aboveground biomass for forest carbon monitoring system in the tri-state region of Maryland, Pennsylvania and Delaware, USA. Environ. Res. Lett. 14, 095002.

Hudak, A.T., Strand, E.K., Vierling, L.A., Byrne, J.C., Eitel, J.U., Martinuzzi, S., Falkowski, M.J., 2012. Quantifying aboveground forest carbon pools and fluxes from repeat lidar surveys. Remote Sens. Environ. 123, 25–40.

Hudak, A.T., Fekety, P.A., Kane, V.R., Kennedy, R.E., Filippelli, S.K., Falkowski, M.J., Tinkham, W.T., Smith, A.M., Crookston, N.L., Domke, G.M., et al., 2020. A carbon monitoring system for mapping regional, annual aboveground biomass across the northwestern USA. Environ. Res. Lett. 15, 095003.

IPCC, 2021. Climate Change 2021: The Physical Science Basis. Contribution of Working Group I to the Sixth Assessment Report of the Intergovernmental Panel on Climate Change. Cambridge University Press, Cambridge, United Kingdom and New York, NY, USA.
Kennedy, R.E., Yang, Z., Cohen, W.B., 2010. Detecting trends in forest disturbance and recovery using yearly landsat time series: 1. Landtrendr — temporal segmentation algorithms. Remote Sens. Environ. 114, 2897–2910.
Kerchner, C.D., Keeton, W.S., 2015. California's regulatory forest carbon market: viability for northeast landowners. Forest Policy Econ. 50, 70–81.
Kriegeskorte, N., Lindquist, M.A., Nichols, T.E., Poldrack, R.A., Vul, E., 2010. Everything you never wanted to know about circular analysis, but were afraid to ask. J. Cereb. Blood Flow Metab. 30, 1551–1557.
Lister, A.J., Andersen, H., Frescino, T., Gatziolis, D., Healey, S., Heath, L.S., Liknes, G.C., McRoberts, R., Moisen, G.G., Nelson, M., Riemann, R., Schleeweis, K., Schroeder, T. A., Westfall, J., Wilson, B.T., 2020. Use of remote sensing data to improve the efficiency of national forest inventories: a case study from the United States national forest inventory. Forests 11.
Liu, Z., Peng, C., Work, T., Candau, J.N., Desrochers, A., Kneeshaw, D., 2018. Application of machine-learning methods in forest ecology: recent progress and future challenges. Environ. Rev. 26, 339–350.
Mascaro, J., Asner, G.P., Knapp, D.E., Kennedy-Bowdoin, T., Martin, R.E., Anderson, C., Higgins, M., Chadwick, K.D., 2014. A tale of two "forests": random forest machine learning aids tropical forest carbon mapping. PLoS One 9, e85993.
McConville, K.S., Moisen, G.G., Frescino, T.S., 2020. A tutorial on model-assisted estimation with application to forest inventory. Forests 11, 244.
McRoberts, R.E., 2010. Probability- and model-based approaches to inference for proportion forest using satellite imagery as ancillary data. Remote Sens. Environ. 114, 1017–1025.
Millard, K., Richardson, M., 2015. On the importance of training data sample selection in random forest image classification: a case study in peatland ecosystem mapping. Remote Sens. 7, 8489–8515.
Næsset, E., 2011. Estimating above-ground biomass in young forests with airborne laser scanning. Int. J. Remote Sens. 32, 473–501.
Olden, J.D., Lawler, J.J., Poff, N.L., 2008. Machine learning methods without tears: a primer for ecologists. Source: Q. Rev. Biol. 83, 171–193.
Rao, J.N., Molina, I., 2015. Small Area Estimation. John Wiley & Sons.
Reinhardt, E., Crookston, N.L., 2003. The Fire and Fuels Extension to the Forest Vegetation Simulator. Gen. Tech. Rep. RMRS-GTR-116.. U.S. Department of Agriculture, Forest Service, Rocky Mountain Research Station, Ogden, UT, 209 p., 116.
Rogan, J., Franklin, J., Stow, D., Miller, J., Woodcock, C., Roberts, D., 2008. Mapping land-cover modifications over large areas: a comparison of machine learning algorithms. Remote Sens. Environ. 112, 2272–2283.
Saarela, S., Grafström, A., Ståhl, G., Kangas, A., Holopainen, M., Tuominen, S., Nordkvist, K., Hyyppä, J., 2015. Model-assisted estimation of growing stock volume using different combinations of lidar and landsat data as auxiliary information. Remote Sens. Environ. 158, 431–440.
Segal, M.R., 2004. Machine Learning Benchmarks and Random Forest Regression.
Shimada, M., Itoh, T., Motooka, T., Watanabe, M., Shiraishi, T., Thapa, R., Lucas, R., 2014. New global forest/non-forest maps from alos palsar data (2007–2010). Remote Sens. Environ. 155, 13–31.
Silva, C.A., Duncanson, L., Hancock, S., Neuenschwander, A., Thomas, N., Hofton, M., Fatoyinbo, L., Simard, M., Marshak, C.Z., Armston, J., Lutchke, S., Dubayah, R., 2021. Fusing simulated gedi, icesat-2 and nisar data for regional aboveground biomass mapping. Remote Sens. Environ. 253, 112234.
Simard, M., Pinto, N., Fisher, J.B., Baccini, A., 2011. Mapping forest canopy height globally with spaceborne lidar. J. Geophys. Res. Biogeosci. 116, 4021.
Stein, M., 1999. Interpolation of Spatial Data: Some Theory for Kriging. In: Springer Series in Statistics. Springer, New York.
Streck, C., 2021. How voluntary carbon markets can drive climate ambition. J. Energy Nat. Resourc. Law 39, 367–374.
Strunk, J., Temesgen, H., Andersen, H.E., Flewelling, J.P., Madsen, L., 2014. Effects of lidar pulse density and sample size on a model-assisted approach to estimate forest inventory variables. Can. J. Remote. Sens. 38, 644–654.
Temesgen, H., Ver Hoef, J.M., 2015. Evaluation of the spatial linear model, random forest and gradient nearest-neighbour methods for imputing potential productivity and biomass of the pacific northwest forests. Forestry Int. J. For. Res. 88, 131–142.
Turkkan, N., Pham-Gia, T., 1993. Computation of the highest posterior density interval in Bayesian analysis. J. Stat. Comput. Simul. 44, 243–250.
Urbazaev, M., Thiel, C., Cremer, F., Dubayah, R., Migliavacca, M., Reichstein, M., Schmullius, C., 2018. Estimation of forest aboveground biomass and uncertainties by integration of field measurements, airborne lidar, and sar and optical satellite data in mexico. Carb. Balance Manag. 13, 1–20.
Ver Hoef, J., 2002. Sampling and geostatistics for spatial data. Ecoscience 9, 152–161.
White, G.W., McConville, K.S., Moisen, G.G., Frescino, T.S., 2021. Hierarchical bayesian small area estimation using weakly informative priors in ecologically homogeneous areas of the interior western forests. Front. Forests Global Change 4. https://doi.org/10.3389/ffgc.2021.752911.
Wojcik, O.C., Olson, S.D., Nguyen, P.H.V., McConville, K.S., Moisen, G.G., Frescino, T.S., 2022. Gregory: a modified generalized regression estimator approach to estimating forest attributes in the interior western us. Front. Forests Global Change 4. https://doi.org/10.3389/ffgc.2021.763414.
Zhang, Y., Liang, S., 2020. Fusion of multiple gridded biomass datasets for generating a global forest aboveground biomass map. Remote Sens. 12.